



UNIVERSITÀ DEGLI STUDI DI TORINO

This is an author version of the contribution published on:

Dario L. Longo, Antonietta Bartoli, Lorena Consolino, Paola Bardini,

Francesca Arena, Markus Schwaiger, and Silvio Aime

In vivo imaging of tumor metabolism and acidosis by combining PET and MRI-CEST
pH imaging.

In Cancer Res. 2016, 76, 6463

The definitive version is available at:

DOI: 10.1158/0008-5472.CAN-16-0825

In vivo imaging of tumour metabolism and acidosis by combining PET and MRI-CEST pH imaging in a breast cancer model

Dario L. Longo ^{1,2}, Antonietta Bartoli ², Lorena Consolino ^{2,3}, Paola Bardini^{2,3}, Francesca Arena^{2,3}, Markus Schwaiger ⁴ and Silvio Aime ^{2,3*}

¹ Institute of Biostructure and Bioimaging (CNR) c/o Molecular Biotechnologies Center, Via Nizza 52, 10126, Torino, Italy

² Molecular Imaging Center, University of Torino, Via Nizza 52, 10126 Torino, Italy

³ Department of Molecular Biotechnology and Health Sciences, University of Torino, Via Nizza 52, 10126 Torino, Italy

⁴ Technische Universität München, Klinikum rechts der Isar, Department of Nuclear Medicine, Ismaninger Str. 22, 81675 München, Germany

Running title: pH and ¹⁸F-FDG MRI/PET tumour imaging

Keywords: ¹⁸F-FDG PET; tumour pH; MRI-CEST; pH imaging; breast cancer;

Grant Support

Financial support from TUM-IAS (Hans Fisher Senior Fellowship to SA), from European Community `s Seventh Framework Programme (FP7 GLINT project 602306) and from Deutsche Forschungsgemeinschaft (DFG project SFB 824) is gratefully acknowledged.

***Corresponding author:**

Silvio Aime, Dipartimento di Biotecnologie Molecolari e Scienze per la Salute, Università degli Studi di Torino

Via Nizza 52, 10126, Torino, Italy.

e-mail: silvio.aime@unito.it, Phone: +39-011-6706451, Fax: +39-011-6706487

Disclosure of Potential Conflict of Interest

The authors declare that they have no conflict of interest.

word count: 4105

total number of tables and figures: 6

ABSTRACT

The vast majority of cancer exhibit increased glucose uptake and glycolysis regardless of oxygen availability. This metabolic shift leads to an enhanced production of lactic acid that, in turn, leads to the acidification of the extracellular pH (pHe) which represents a characteristic hallmark of tumour microenvironment. Dysregulated tumour pHe and up-regulated glucose metabolism are therefore tightly linked and their relative assessment may be very useful for pursuing a better understanding of the underlying biology. Here we investigated *in vivo* and non-invasively the correlation between tumour ^{18}F -FDG uptake and extracellular pH values in a breast HER2+ tumour murine model. Tumour extracellular pH and perfusion have been assessed by acquiring MRI-CEST (Chemical Exchange Saturation Transfer) images on a 3T scanner, upon the intravenous administration of a pH-responsive contrast agent (iopamidol). Static PET images were recorded immediately after MRI acquisitions to quantify the extent of ^{18}F -FDG uptake. First, we demonstrated accurate tumour pHe measurements that were able to report on induced pHe changes. Combined PET and MRI-CEST images reported complementary spatial information of the altered glucose metabolism. A significant inverse correlation was found between extracellular tumour pH and ^{18}F -FDG uptake (%ID/g: $r = -0.552$, $P < 0.01$; SUV: $r = -0.587$, $P < 0.01$). Furthermore, for the first time, we demonstrated *in vivo* that tumours with high ^{18}F -FDG uptake show higher extracellular acidosis. These results suggest that merging the information between ^{18}F -FDG-uptake and extracellular pH mapping represent a valuable tool for an improved imaging-based characterisation of tumour microenvironment.

INTRODUCTION

Solid tumours are characterized by a highly heterogeneous and acidic microenvironment. The combination of poor vascular perfusion, regional hypoxia and high rates of glucose metabolism are responsible for generating extracellular acidosis in solid tumours (1). In fact, tumour cells rely mostly on the conversion of glucose into lactate rather than mitochondrial oxidation for energy production, even in the presence of well-oxygenated conditions (Warburg effect) (2). This metabolic switch toward a glycolytic phenotype occurs early in cancers, during the avascular phase, thus promoting the adaptation of the tumour cells to an acidic microenvironment. Extracellular tumour acidosis is an indicator of bad prognosis and it is relevant to facilitate tumour migration and invasion by the degradation of the extracellular matrix (3). Tumour acidosis has also been linked to multi-drug resistance due to the neutralization of weak base chemotherapeutic drugs, which makes the drugs less efficient to cross the cellular membrane (4). It follows that the possibility of measuring precise extracellular tumour pH (pHe) at high spatio-temporal resolution is considered of great interest in both preclinical and clinical settings, offering selective and specific strategies for developing new treatments for solid tumours (5, 6). Moreover, the development quantitative imaging techniques and novel imaging biomarkers is considered a key research priority in the medical imaging community (7, 8).

Currently the gold standard for tumour detection in clinical settings is represented by [¹⁸F]2-fluoro-2-deoxy-D-glucose (¹⁸F-FDG) as it acts as a metabolic tracer in positron emission tomography (PET) to report on the over-expression/up-regulation of glucose transporters (9). ¹⁸F-FDG enters the tumour cells and accumulates because it cannot be metabolised beyond the first phosphorylation step. In spite of the complexity of the ¹⁸F-FDG PET methodology, ¹⁸F-FDG quickly became a biomarker of outstanding importance in oncology and it is used daily in the clinical settings as a surrogate marker of pathological response and survival for a vast array of cancers (10). Despite this valuable functional information, PET imaging suffers for a limited spatial resolution that limits the information about tumour heterogeneity (11). Conversely, the superb spatial resolution of magnetic resonance imaging (MRI) allows accurate assessments of the heterogeneity of the tumour lesion. Several MRI-based approaches have been proposed for measuring tumour pH *in vivo* (12-14). Among them, the method based on chemical exchange saturation transfer (CEST) has recently gained great attention (15). This MRI approach relies on the pH-dependence of the prototropic exchange rates and the

exchange of magnetization between mobile protons and water is exploited for detecting low-concentration molecules. As a source of mobile protons, either endogenous amide-containing molecules (16, 17), or exogenous pH-responsive contrast agents (CAs) can be used (18-20). Notably, within the latter class, it has been shown that the FDA-approved iodinated contrast media for x-ray computed tomography (CT) imaging can be exploited for MRI-CEST pH imaging both at preclinical and clinical level (19, 21-24).

Currently, there is a great expectation that the combination of PET and MRI techniques in the acquisition of images of the same anatomical region may open new horizons for an improved characterisation of tumour microenvironment, merging functional information delivered by PET with morphologic and functional imaging attainable by MRI. The physical integration of PET and MRI systems has already been achieved both for clinical use as well as for animal studies (25, 26). Therefore, by integrating MRI/PET information, the advantages of each imaging modality for assessing key features of the pathology can be exploited (27, 28). In addition, reduction of ionizing radiation dose, in comparison to PET/ CT systems, gives further support to consider PET/MRI approaches especially in longitudinal studies.

In general, one would expect that tumour extracellular pH and ^{18}F -FDG uptake are linked as the lowering of pH in the extracellular region is, first of all, the result of an increased production of glycolytic byproducts, lactate and H^+ , which are released by cancer cells in order to maintain physiological intracellular pH homeostasis (29). It is therefore important to elucidate, for each tumour phenotype, whether and to what extent, ^{18}F -FDG uptake and pHe can be closely-lined biomarkers of the altered glycolytic rate. Unfortunately, despite aerobic glycolysis and increased extracellular acidification are recognised as hallmarks of solid tumours, no clear evidence of this relationship has been reported so far *in vivo*. In addition, it would be desirable to develop imaging approaches that can be translatable to the clinics. Here we assess the potential of MRI-CEST tumour pHe mapping at a clinical field of 3T by using the pH-responsive contrast agent iopamidol. We show that the combination of ^{18}F -FDG PET uptake and iopamidol-based MRI-CEST pH mapping can provide new insights for an improved characterisation of tumour metabolism and microenvironment.

MATERIALS AND METHODS

Materials

The following materials were used in this study: RPMI1640 medium, fetal bovine serum, glutamine, penicillin and streptomycin (Lonza Sales AG, Verviers, Belgium); Iopamidol (Bracco Imaging Spa, Colliero Giasosa, Italy); ¹⁸F-FDG (Advanced Acceleration Applications, Colliero Giasosa, Italy); phosphate-saline buffer (Sigma Aldrich, Milano, Italy); goat serum (Sigma Aldrich, Milano, Italy); O.C.T. compound (Tissue Tek®, Sakura Finetek, Tokyo, Japan); primary antibody rat anti-mouse CD31 (BD Pharmigen, Milano, Italy); secondary antibody Alexa Fluor-568 goat anti-rat (Life Technologies, Monza, Italy); Hoescht33258 (Sigma Aldrich, Milano, Italy); mounting medium Fluoroshield (Sigma Aldrich, Milano, Italy).

Tumour Model

TS/A is an aggressive and poorly immunogenic cell line first established from the *in vivo* transplant of a moderately differentiated mammary adenocarcinoma that arose spontaneously in a 20-month-old multiparous BALB/c mouse (30). TS/A cells were maintained in RPMI 1640 medium supplemented with 10% fetal bovine serum, 2mM glutamine, 100 U/mL penicillin and 100 µg/mL streptomycin and preserved in a humidified incubator at 37°C with 5% CO₂. For the preparation of the TS/A tumour model, 2.5x10⁵ cells in RPMI medium were inoculated subcutaneously into both the left and right hind limb of BALB/c mice, respectively. Tumour growth was allowed to grow to 3 to 5 weeks into tumours of suitable volume that was precisely measured by MRI. To investigate the relationship between glucose uptake and tumour pHe, a first cohort of TS/A tumour bearing mice were imaged by sequential MRI and PET imaging (n=23 tumours). An additional cohort of TS/A bearing mice were split into two groups, with the first group receiving 200 mM bicarbonated water ad libitum for five days to modulate tumour pHe (n=6), and the second group receiving regular drinking water (n=6). All animal procedures and husbandry were performed in accordance with the

European Communities Council Directive (86/609/EEC) and approved by the Committee on Animal Care and Use of our University.

MRI-CEST experiments

MR images were acquired on a 3T Bruker Biospec (Bruker, Ettlingen Germany) scanner equipped with a 30 mm quadrature RF coil. Mice were anaesthetised with isoflurane vaporised with O₂. Isoflurane was used at 3.0% for induction and at 1.0%–2.0% for maintenance. A single T₂-weighted axial slice crossing the centre of the tumours was acquired with TR = 4 sec, TE = 3.7 ms, NA = 1, slice thickness = 1.5 mm, FOV = 30x30 mm, matrix size = 256x256, which yielded an in-plane resolution of 117 μm. CEST images were acquired with continuous wave (CW) RF irradiation (3 μT for 5 sec) by using a single-shot RARE sequence (TR = 6.0 sec, effective TE = 8.7ms, centric encoding, slice thickness = 1.5 mm, FOV = 30 mm, matrix size = 96x96, in-plane spatial resolution = 312 μm, NA = 1) with 46 frequency offsets unevenly distributed from -10 to 10 ppm relative to the water resonance, with the acquisition time for each Z-spectrum being 4 min 36s. The contrast agent (iopamidol) was injected intravenously into the tail vein at a dose of 4 g I/kg b.w. for tumour pH mapping.

PET imaging and analysis

Following the MRI, a dedicated animal bed was designed to immediately shift the mice to the PET scanner (for a similar approach see (31)), where static acquisitions were performed after an uptake time of 45 min and a ¹⁸F-FDG injected dose of 15±3 MBq. MRI and PET/CT images were coregistered by fiducial markers. Mice were anaesthetized with isoflurane vaporized with O₂. Isoflurane was used at 3.0% for induction and at 1.0%–2.0% for maintenance. Mice were imaged using the trimodality PET/SPECT/CT scanner Triumph (Trifoil imaging, Chatsworth, CA, USA). ¹⁸F-FDG was supplied by Advanced Accelerator Applications (AAA, Colleretto Giacosa, Italy). Mice were kept fasting overnight before intravenously ¹⁸F-FDG injection. PET images were acquired 45 min after tracer injection followed by a CT acquisition (80 kVp, 110 mA, magnification 2.25). PET data were reconstructed using 2D-Maximum Likelihood Expectation

Maximization (MLEM) algorithm with 10 iterations and were corrected for tracer decay and for photon attenuation. Analysis of PET images and co-registration to MR images were performed using PMOD software (<http://www.pmod.com>). A volume-of-interest (VOI) approach was used to determine the amount of radiotracer uptake and to determine regional values for the maximal percentage injected dose per cubic centimeter (%ID/cm³). The SUV and SUVmax were obtained using the following formula: SUV = mean activity in the region of interest (MBq/g)/(injected dose [MBq]/body weight) and SUVmax: maximum activity in the region of interest (MBq/g)/(injected dose [MBq]/body weight).

CEST image analysis

All data analysis was performed using custom-written scripts in Matlab (Mathworks, Natick, MA, USA). All Z-spectra were interpolated, on a voxel-by-voxel basis, by smoothing splines, to identify the right position of the bulk water signal, for B₀ inhomogeneity correction. The interpolated Z-spectrum was shifted so that the bulk water resonance corresponds to the zero frequency and CEST contrast was quantified at a specific offset of interest (i.e. Δω = +4.2/+5.5 ppm) using the asymmetry analysis:

$$ST = \frac{S_{-\Delta\omega} - S_{+\Delta\omega}}{S_0}$$

Where S_{±Δω} is the water signal intensity in the presence of a saturation pulse at offset ±Δω and S₀ is water signal intensity in the absence of a saturation pulse.

For *in vivo* images, difference contrast maps (ΔST%) were calculated by subtracting the ST% contrast after iopamidol injection from the ST% contrast before the injection on a per voxel basis in order to reduce the confounding effect of the endogenous contributions. ST% maps were calculated for both the frequency offsets of 4.2 and 5.5 ppm, by subtracting the corresponding pre-contrast ST% maps. A threshold value of 2% was set, based on the ΔST variations between multiple pre-contrast ST% maps (ca. 0.8% at 4.2 ppm and 1.7% at 5.5 μT, respectively) to discriminate between enhancing and not-enhancing pixels. Ratiometric values were calculated by ratioing the difference contrast maps at the two different frequency offsets of 4.2 and 5.5 ppm. Only those voxels showing an increase of ST contrast higher than 2%, in comparison to pre-

contrast ST% map were included for the following pH calculations. pH maps were obtained by back-calculating the pH values from the obtained ratiometric values on a voxel-by-voxel basis according to the corresponding pH calibration curve of Fig. 1c. Extravasation (perfusion) maps were determined as the percentage of pixels showing a Δ ST% higher than 2% inside the whole tumour region. The higher the percentage of pixels showing an increase of the ST% contrast above the threshold, the higher the corresponding extravasation parameter.

Histologic analysis

After images acquisition, mice were sacrificed and tumour tissues excised. Tumours were embedded in O.C.T. compound and frozen in liquid nitrogen. Cryo-sections slices of 5 μ m of thickness were subsequently cut and fixed in ice-cold acetone for 10 minutes and blocked with PBS containing 10% goat serum for 1 hour at room temperature. The sections were incubated with anti-mouse CD31 (1:200) overnight and then with secondary antibody (1:500) for 1 hour at room temperature. After nuclei staining with Hoescht 33258 for 10 minutes at room temperature, sections were mounted with Fluoroshield. Images were acquired with a motorised z-focus confocal microscope (Leica Microsystems, Milano, Italy).

Statistical analysis

Statistical evaluations were performed using GraphPad Prism software (GraphPad, San Diego, CA, USA). Correlations among MRI-CEST (using pH, Δ ST% and extravasation fraction) and 18 F-FDG-PET (using %ID/g, SUV and SUVmax) values and tumour volumes were calculated using the Pearson product-moment coefficient. Correlations were interpreted using the guidelines from Cohen (32), with absolute correlations of <0.3 considered weak, 0.3–0.5 moderate, and 0.5–1.0 strong. Statistical significance was assessed at a level of P less than 0.05.

RESULTS

The CEST method for mapping pH using iopamidol (a widely used x-ray contrast agent) was recently proposed and applied *in vivo* on a scanner operating at 7 T (18). As our project aims at exploring routes to transfer preclinical results to clinical applications it was deemed of interest to work at 3T that is the magnetic field strength of the currently available PET-MRI scanners. Iopamidol MRI-CEST pH-sensitivity was then first evaluated at 3T and 310K on a phantom consisting of tubes filled with aqueous solutions of Iopamidol (30mM) at different pH, from 6.0 to 7.4. The Saturation Transfer (ST%) values to the bulk water signal were measured when the off-set of the irradiation fields was set at the exchanging amide proton resonances, i.e, at 4.2 ppm and at 5.5 ppm, respectively. Fig. 1a shows representative Z-spectra at pH of 6, 6.5 and 7. Fig. 1b shows CEST effect (ST%) measured at 4.2 (circles) and 5.5 (squares) ppm, respectively, upon applying a saturation rf field of 3 μ T for 5s. ST% values steadily increase with pH for both amide proton pools. The differences in the pH dependence of ST% observed for the absorptions at 4.2 and 5.5 ppm enables the set-up of the ratiometric method for pH quantification yielding ratios that range from 1.1 to 1.9 on going from pH 6 to 7.4, respectively (Fig. 1c). The accuracy of the pH-CEST method was evaluated by comparing the pH values calculated on the basis of the observed ST% ratios and the pH values measured by a pH-meter. pH values determined from the MRI-CEST approach strongly correlates with the calibrated pH (Pearson's $r = 0.993$, $P < 0.001$), showing that a good pH accuracy is feasible at a clinical magnetic field. The pH MRI precision decreased with pH, as the standard deviation of calculated pH was higher at lower pH, likely due to the decreased prototropic exchange rates at lower pH that results in smaller ST% effects (Fig. 1d).

MRI-CEST pH maps were acquired *in vivo* in HER2 positive tumour bearing mice upon the intravenous administration of iopamidol at clinical magnetic field (3T). CEST contrast was quantified by measuring difference ST% maps (Δ ST% = ST%_{post} – ST%_{pre} iopamidol injection) in order to reduce confounding effects from baseline ST contrast arising from tumour endogenous components. It has been found that iopamidol is sufficiently well detected at this field, with an average ST% increase from baseline values of 3-5% at 4.2 ppm and of 2-4% at 5.5 ppm, respectively (Fig. 2e). Δ ST% maps showed that the increase in ST% contrast is highly heterogeneous in the ROI, indicating that not all the voxels of the tumour region are vascularised, or are leaky, to a similar extent (Fig. 2a and Fig. 2b). As a consequence, the not homogeneous distribution of iopamidol is itself a read-out of the extent of perfusion in the tumour microenvironment and it directly informs about the tumour heterogeneity in terms of vascular permeability (Fig. 2d). Overall, about

50-60% of the total pixels showed an increase in $\Delta ST\%$ values above the detection thresholds. For these pixels the corresponding tumour extracellular pH values have been computed (Fig. 2c). All the investigated HER2 positive breast cancer mice showed extracellular acidifications, with mean tumour extracellular pH values in the range 6.6-7.0. Variations in pHe values within the tumours covered a range of ~ 0.6 -0.8 pH units (Fig. 2c), but no marked general trend (e.g. from the core to the rim) was observed.

Validation of the proposed CEST-pH mapping approach in assessing pHe changes was performed in tumours bearing mice fed with bicarbonated water. The average pHe in control mice was significantly more acidic than the average pHe of tumours in mice having received 5 days of bicarbonated water (6.74 ± 0.07 versus 7.01 ± 0.08 , respectively; $P < 0.001$, Fig. 3a). Representative tumour pHe maps show an increase of less acidic pHe voxels in mice drinking water containing sodium bicarbonate, in comparison to control mice (Figs. 3b and 3c).

Fig. 4 shows one example of a mouse bearing subcutaneous HER2+ allograft tumours, which was sequentially imaged by a 3T MRI and a PET scanner. After the acquisition of tumour pHe map upon iopamidol injection (Fig. 4a), the ^{18}F -FDG tracer was administered and static PET images were acquired, clearly showing ^{18}F -FDG uptake in the tumour regions (Fig. 4b). The area of higher FDG uptake in the tumour corresponds to lower pHe values, whereas the area of lower FDG uptake corresponds to less acidic tumour microenvironment. This can also be seen in the histogram analysis of the corresponding areas, showing pHe distribution values shifted to more acidic values for the tumour regions with an increased glucose uptake (Fig. 4c). In the analyzed tumors, the ^{18}F -FDG average %ID/g ranged from 1.5 to 5.5% (mean $3.2 \pm 1.1\%$), the SUV ranged from 0.4 and 1 (mean 0.7 ± 0.2) and the SUVmax ranged from 0.5 to 1.3 (mean 0.9 ± 0.3).

Finally, the relationship between the glycolytic rate and tumour acidosis was assessed between the estimates obtained from ^{18}F -FDG-PET and MRI-CEST pH in 23 matched PET-MRI tumour images (Table 1 and Fig. 5). PET derived parameters appear related to the tumour volume (Pearson's correlation coefficients %ID/g: $r = -0.671$, $P < 0.01$; SUV: $r = -0.710$, $P < 0.01$, SUVmax: $r = -0.764$, $P < 0.01$; TLG: $r = 0.467$, $P < 0.01$). A significantly strong correlation was found between ^{18}F -FDG uptake related parameters and CEST-pH measurements (%ID/g: $r = -0.552$, $P < 0.01$, SUV: $r = -0.587$, $P < 0.01$ and SUVmax: $r = -0.525$, $P < 0.01$).

Insights on the heterogeneous tumour vascularisation have been gained ex-vivo by immunofluorescence staining for CD-31 which showed an extensive tumour vascular heterogeneity (Supplementary Fig. S1) analogous to that measured by CEST extravasation maps (Fig. 2d).

DISCUSSION

To the best of our knowledge, this is the first study aimed at comparing ^{18}F -FDG uptake and extracellular pH in tumours by means of combined PET and MRI-CEST measurements. The herein reported results show that this approach is feasible and it may be a valuable tool for non-invasive imaging-based metabolic phenotyping of tumours.

^{18}F -FDG-PET imaging is a well established, clinically used modality in the diagnosis and management of various malignancies, showing that the vast majority of cancers exhibit significantly increased glucose uptake compared with normal tissue. The increased glycolysis of tumour cells, even in the presence of adequate oxygen supplies, results in a significant decrease of the extracellular pH. There is now good evidence that the increased consumption of glucose is instrumental for the production of H^+ , which promotes tumour cell migration, invasion and angiogenesis (33). Increased glucose consumption and increased acid production are therefore tightly correlated and their relative assessment may be very useful for pursuing a better understanding of the underlying biology. The herein reported results show that a good correlation exists between ^{18}F -FDG-PET uptake (associated with the metabolic characteristics of the tumour) and MRI-CEST extracellular pH (associated with the acidification of the extracellular tumour microenvironment). In the investigated breast tumour model, we observed a significant inverse correlation between ^{18}F -FDG uptake and extracellular pH (Fig. 5). Moreover, it has been found that tumour regions with higher extracellular acidosis correspond to tumour regions with high ^{18}F -FDG uptake (Fig. 4c). Notably, the observed behaviour is in agreement with the expectation that glycolysis and production of acids are increased in tumour cells compared to normal cells (34). Previous studies investigated the relationship between tumour acidosis and lactate production, but no spatial correlations have been observed, despite large amount of lactate are excreted by glycolytic cancer cells (13, 35). One possible explanation is related to the role of lactate in

tumour metabolism, for which recent findings have shown that is not merely the final product of glycolysis, but it can be re-used as an energetic fuel for oxidative metabolism (36). Therefore, the lack of a direct correlation between lactate and acidosis may not be unexpected accordingly to the differential use of this molecule.

Interest in measuring and *in vivo* imaging of tumour pH has driven the development of pH-sensing contrast agents, in particular in the MRI field, in order to obtain pH maps of both extracellular and intracellular compartments (5, 14, 37). MRI-CEST based approaches have recently emerged as a powerful tool for imaging pH, thanks to the development of ratiometric methods that rule out the need to know the contrast agent concentration (18, 22, 38-40). In addition, our approach, in comparison to others, allow measurements of tumour pHe with high spatial resolution, high temporal resolution and can be applied to tumours as small as few mm³ (41). Cancers display various kinds of heterogeneity, including metabolism and vasculature, but many approaches are limited to volume-averaged tumour pHe measurements that cannot account for tumour heterogeneity (42). In contrast, CEST-pH imaging allows the non-invasive characterisation of *in vivo* pHe distribution on a voxel-basis. Owing to the high spatial resolution of MRI-CEST images, the pHe values distribution within a tumour ROI can also be analysed by conventional histogram analysis as an improved method to assess pHe heterogeneity (Fig. 4c). Our technique, owing to the injection of an extracellular agent, allows also the assessment of the extravasation fraction, a surrogate marker of tumour perfusion. We observed inhomogeneous iopamidol distribution within the tumours, likely reflecting low and high vascularised area in the heterogeneous tumour region, as confirmed by immunohistochemical analysis of tumour vascularisation (Supplementary Fig. S1). Similar findings have also been reported upon comparing several iodinated contrast media, in the same breast tumour model (43). It was found that the heterogeneous distribution of x-ray radiographic molecules in the extracellular-extravascular space of the tumour, as measured by the CEST approach, correlates well with the extravasation quantified by the CT approach, hence dependent on tumour vascular volume and vessel permeability characteristics.

Besides the capability of measuring tumour pHe, novel proposed approaches should be able to provide a precise read-out of pH changes. It is known that administering sodium bicarbonate significantly alter tumour pHe (44). We achieved similar results with mice drinking *ad libitum* bicarbonate water (200 mM): the

average tumour pHe in the non-modulated mice was significantly more acidic than the average pHe of tumours in mice having received 5 days of bicarbonated water (Fig. 3). Thus our approach is enough sensitive to detect small pHe changes upon pharmacological treatment, thus opening the possibility to exploit pH imaging as a surrogate marker of therapeutic response to novel anticancer therapies (45).

Overall, as the information provided by each readout (^{18}F -FDG uptake and pH) reflect a different aspect of the same altered metabolic behaviour, the combination of the two metrics should results in a synergic action of the two modalities. Furthermore, the availability of combined PET/MRI scanners for the simultaneous acquisition of molecular and functional data with high temporal and spatial fusion accuracy are already available both at preclinical and clinical level, thus making pH mapping and ^{18}F -FDG uptake a powerful tool for tumour metabolic phenotyping (46, 47). However, despite the extracellular acidity is considered a distinctive feature of cancer, the exploitation of pH sensing agents has been commonly limited to preclinical studies, since no investigations on their safety profiles have been reported so far for their use in patients. On the contrary, the method presented here uses a pH-responsive agent that is a FDA approved contrast media within the CT modality, hence a fast translation to patients for assessing tumour pH is expected; in fact, an early phase clinical trial to estimate tumour extracellular pH in women with early stage breast cancer is currently ongoing (48). Moreover, analogues approaches based on other (radio)-tracers specific for physiological processes such as proliferation, hypoxia and amino acid transporters may likely widen the impact of hybrid PET/MRI measurements for tumour characterisation (49, 50).

One of the limitations of our study is that pH and ^{18}F -FDG measurements have been performed on the same animal but not simultaneously on the same scanner, therefore the time gap between the two measures may likely introduce some bias on the metrics that we are comparing. However, the aim of this study was the correlation between the mean tumour values of ^{18}F -FDG uptake and pHe, and further combined MRI/PET studies will allow investigating the true temporal and spatial correlation between the two estimates.

CONCLUSION

In summary, the herein reported results, although limited to a breast cancer murine model, have shown the correlation between tumour extracellular pH and ^{18}F -FDG uptake. MRI-CEST tumour pH mapping provides significant, complementary information to ^{18}F -FDG-PET in the characterisation of the cancer phenotype, as the high spatial resolution associated to MR images provides additional insights on tumour perfusion heterogeneity. Furthermore, as the increased acidification of the extracellular tumour microenvironment can be targeted with specific novel therapies, this combined imaging approach could be exploited as a novel imaging biomarker of therapeutic response.

Authors' Contributions

Conception and design: S. Aime, D.L. Longo, M. Schwaiger

Development of methodology: D.L. Longo, A. Bartoli

Acquisition of data (provided animals, acquired images): D.L. Longo, L. Consolino, A. Bartoli, P. Bardini, F. Arena

Analysis and interpretation of data: D.L. Longo, L. Consolino, A. Bartoli, P. Bardini, F. Arena

Writing, review and/or revision of the manuscript: D. Longo, A. Bartoli, M. Schwaiger, S. Aime

Study supervision: S. Aime

REFERENCES

1. Damaghi M, Wojtkowiak JW, Gillies RJ. pH sensing and regulation in cancer. *Front Physiol* 2013; 4: 370.
2. Warburg O. On the origin of cancer cells. *Science* 1956; 123: 309-14.
3. Gatenby RA, Gawlinski ET. A reaction-diffusion model of cancer invasion. *Cancer Res* 1996; 56: 5745-53.
4. Sauvant C, Nowak M, Wirth C, et al. Acidosis induces multi-drug resistance in rat prostate cancer cells (AT1) in vitro and in vivo by increasing the activity of the p-glycoprotein via activation of p38. *Int J Cancer* 2008; 123: 2532-42.
5. Zhang X, Lin Y, Gillies RJ. Tumor pH and its measurement. *J Nucl Med* 2010; 51: 1167-70.
6. De Milito A, Fais S. Tumor acidity, chemoresistance and proton pump inhibitors. *Future Oncol* 2005; 1: 779-86.
7. Bernsen MR, Kooiman K, Segbers M, van Leeuwen FW, de Jong M. Biomarkers in preclinical cancer imaging. *Eur J Nucl Med Mol Imaging* 2015; 42: 579-96.
8. Winfield JM, Payne GS, deSouza NM. Functional MRI and CT biomarkers in oncology. *Eur J Nucl Med Mol Imaging* 2015; 42: 562-78.
9. Shaw RJ. Glucose metabolism and cancer. *Curr Opin Cell Biol* 2006; 18: 598-608.
10. Rohren EM, Turkington TG, Coleman RE. Clinical applications of PET in oncology. *Radiology* 2004; 231: 305-32.
11. Wehrl HF, Wiehr S, Divine MR, et al. Preclinical and Translational PET/MR Imaging. *J Nucl Med* 2014; 55: 11S-8S.
12. Raghunand N, Zhang S, Sherry AD, Gillies RJ. In vivo magnetic resonance imaging of tissue pH using a novel pH-sensitive contrast agent, GdDOTA-4AmP. *Acad Radiol* 2002; 9 Suppl 2: S481-3.
13. Gallagher FA, Kettunen MI, Day SE, et al. Magnetic resonance imaging of pH in vivo using hyperpolarized ¹³C-labelled bicarbonate. *Nature* 2008; 453: 940-3.
14. Perez-Mayoral E, Negri V, Soler-Padros J, Cerdan S, Ballesteros P. Chemistry of paramagnetic and diamagnetic contrast agents for Magnetic Resonance Imaging and Spectroscopy pH responsive contrast agents. *Eur J Radiol* 2008; 67: 453-8.
15. van Zijl PC, Yadav NN. Chemical exchange saturation transfer (CEST): what is in a name and what isn't? *Magn Reson Med* 2011; 65: 927-48.
16. McVicar N, Li AX, Goncalves DF, et al. Quantitative tissue pH measurement during cerebral ischemia using amine and amide concentration-independent detection (AACID) with MRI. *J Cereb Blood Flow Metab* 2014; 34: 690-8.
17. Sun PZ, Sorensen AG. Imaging pH using the chemical exchange saturation transfer (CEST) MRI: Correction of concomitant RF irradiation effects to quantify CEST MRI for chemical exchange rate and pH. *Magn Reson Med* 2008; 60: 390-7.
18. Longo DL, Dastru W, Digilio G, et al. Iopamidol as a responsive MRI-chemical exchange saturation transfer contrast agent for pH mapping of kidneys: In vivo studies in mice at 7 T. *Magn Reson Med* 2011; 65: 202-11.
19. Chen LQ, Howison CM, Jeffery JJ, Robey IF, Kuo PH, Pagel MD. Evaluations of extracellular pH within in vivo tumors using acidoCEST MRI. *Magn Reson Med* 2013.
20. Delli Castelli D, Ferrauto G, Cutrin JC, Terreno E, Aime S. In vivo maps of extracellular pH in murine melanoma by CEST-MRI. *Magn Reson Med* 2014; 71: 326-32.
21. Longo DL, Busato A, Lanzardo S, Antico F, Aime S. Imaging the pH evolution of an acute kidney injury model by means of iopamidol, a MRI-CEST pH-responsive contrast agent. *Magnetic Resonance in Medicine* 2013; 70: 859-64.
22. Longo DL, Sun PZ, Consolino L, Michelotti FC, Uggeri F, Aime S. A General MRI-CEST Ratiometric Approach for pH Imaging: Demonstration of in Vivo pH Mapping with lobitridol. *J Am Chem Soc* 2014.
23. Sun PZ, Longo DL, Hu W, Xiao G, Wu R. Quantification of iopamidol multi-site chemical exchange properties for ratiometric chemical exchange saturation transfer (CEST) imaging of pH. *Phys Med Biol* 2014; 59: 4493-504.

24. Müller-Lutz A, Khalil N, Schmitt B, et al. Pilot study of iopamidol-based quantitative pH imaging on a clinical 3T MR scanner. *MAGMA* 2014.
25. Gaertner FC, Furst S, Schwaiger M. PET/MR: a paradigm shift. *Cancer Imaging* 2013; 13: 36-52.
26. Sauter AW, Wehrl HF, Kolb A, Judenhofer MS, Pichler BJ. Combined PET/MRI: one step further in multimodality imaging. *Trends Mol Med* 2010; 16: 508-15.
27. Viel T, Talasila KM, Monfared P, et al. Analysis of the growth dynamics of angiogenesis-dependent and -independent experimental glioblastomas by multimodal small-animal PET and MRI. *J Nucl Med* 2012; 53: 1135-45.
28. Haeck JC, Bol K, de Ridder CM, et al. Imaging heterogeneity of peptide delivery and binding in solid tumors using SPECT imaging and MRI. *EJNMMI Res* 2016; 6: 3.
29. Schornack PA, Gillies RJ. Contributions of cell metabolism and H⁺ diffusion to the acidic pH of tumors. *Neoplasia* 2003; 5: 135-45.
30. Nanni P, de Giovanni C, Lollini PL, Nicoletti G, Prodi G. TS/A: a new metastasizing cell line from a BALB/c spontaneous mammary adenocarcinoma. *Clin Exp Metastasis* 1983; 1: 373-80.
31. Bartoli A, Esposito G, D'Angeli L, Chaabane L, Terreno E. MRI and PET Compatible Bed for Direct Co-Registration in Small Animals. *Ieee Transactions on Nuclear Science* 2013; 60: 1596-602.
32. Cohen J. *Statistical power analysis for the behavioral sciences*. 2nd ed. Hillsdale, N.J.: L. Erlbaum Associates; 1988.
33. Gillies RJ, Gatenby RA. Adaptive landscapes and emergent phenotypes: why do cancers have high glycolysis? *J Bioenerg Biomembr* 2007; 39: 251-7.
34. Gatenby RA, Gillies RJ. Why do cancers have high aerobic glycolysis? *Nat Rev Cancer* 2004; 4: 891-9.
35. Garcia-Martin ML, Herigault G, Remy C, et al. Mapping extracellular pH in rat brain gliomas in vivo by 1H magnetic resonance spectroscopic imaging: comparison with maps of metabolites. *Cancer Res* 2001; 61: 6524-31.
36. Payen VL, Porporato PE, Baselet B, Sonveaux P. Metabolic changes associated with tumor metastasis, part 1: tumor pH, glycolysis and the pentose phosphate pathway. *Cell Mol Life Sci* 2015.
37. Aime S, Delli Castelli D, Terreno E. Novel pH-reporter MRI contrast agents. *Angew Chem Int Ed Engl* 2002; 41: 4334-6.
38. Wu R, Longo DL, Aime S, Sun PZ. Quantitative description of radiofrequency (RF) power-based ratiometric chemical exchange saturation transfer (CEST) pH imaging. *NMR Biomed* 2015; 28: 555-65.
39. Sun PZ, Longo DL, Hu W, Xiao G, Wu RH. Quantification of iopamidol multi-site chemical exchange properties for ratiometric chemical exchange saturation transfer (CEST) imaging of pH. *Physics in Medicine and Biology* 2014; 59: 4493-504.
40. Moon BF, Jones KM, Chen LQ, et al. A comparison of iopromide and iopamidol, two acidoCEST MRI contrast media that measure tumor extracellular pH. *Contrast Media Mol Imaging* 2015.
41. Lutz NW, Le Fur Y, Chiche J, Pouyssegur J, Cozzone PJ. Quantitative in vivo characterization of intracellular and extracellular pH profiles in heterogeneous tumors: a novel method enabling multiparametric pH analysis. *Cancer Res* 2013; 73: 4616-28.
42. Vavere AL, Biddlecombe GB, Spees WM, et al. A novel technology for the imaging of acidic prostate tumors by positron emission tomography. *Cancer Res* 2009; 69: 4510-6.
43. Longo DL, Michelotti F, Consolino L, et al. In Vitro and In Vivo Assessment of Nonionic Iodinated Radiographic Molecules as Chemical Exchange Saturation Transfer Magnetic Resonance Imaging Tumor Perfusion Agents. *Invest Radiol* 2016; 51: 155-62.
44. Raghunand N, He X, van Sluis R, et al. Enhancement of chemotherapy by manipulation of tumour pH. *Br J Cancer* 1999; 80: 1005-11.
45. Neri D, Supuran CT. Interfering with pH regulation in tumours as a therapeutic strategy. *Nat Rev Drug Discov* 2011; 10: 767-77.
46. Judenhofer MS, Cherry SR. Applications for preclinical PET/MRI. *Semin Nucl Med* 2013; 43: 19-29.
47. Wehrl HF, Sauter AW, Judenhofer MS, Pichler BJ. Combined PET/MR imaging--technology and applications. *Technol Cancer Res Treat* 2010; 9: 5-20.

48. Arizona Uo. An Early Phase Clinical Trial to Evaluate the Feasibility of CEST MRI in Patients With Early Stage Breast Cancer. Available from: <http://wwwclinicaltrials.gov/ct2/show/NCT02380209>; 2015. p. NLM identifier: NCT02380209.
49. Alberini JL, Boisgard R, Guillermet S, et al. Multimodal In Vivo Imaging of Tumorigenesis and Response to Chemotherapy in a Transgenic Mouse Model of Mammary Cancer. *Mol Imaging Biol* 2015.
50. Penet MF, Krishnamachary B, Chen Z, Jin J, Bhujwala ZM. Molecular imaging of the tumor microenvironment for precision medicine and theranostics. *Adv Cancer Res* 2014; 124: 235-56.

TABLES

Table 1. Pearson correlation coefficients for [¹⁸F]-FDG PET, CEST-pH data and tumour volume

Measures	Volume	%ID/g	SUV	SUVmax	pH	Extravasation
Volume	1					
%ID/g	-0.671**	1				
SUV	-0.710**	0.959**	1			
SUVmax	-0.764**	0.932**	0.952**	1		
pH	0.519**	-0.552**	-0.587**	-0.525**	1	
Extravasation	0.143	0.283	0.208	0.082	-0.025	1

Abbreviations: SUV = mean standard uptake value; SUVmax= maximum SUV.

All correlations were calculated using independent data points from 23 tumours. Intermodality correlations are shown in boldface type.

*p<0.05 **p < 0.01

FIGURE LEGENDS

Fig. 1 Iopamidol pH responsiveness at 3T. (a) Z-spectra of PBS buffered solutions of iopamidol (30 mM) at three representative pH values of 6, 6.5 and 7 ($B_1=3 \mu\text{T}$, RF saturation time = 5s, 310K). (b) CEST ratio (ST%) calculated from the asymmetry analysis as a function of pH. (c) Plot of the ratiometric (R_{ST}) values in the pH range from 6 to 7.4. (d) Comparison of pH values determined by the iopamidol MRI-CEST method versus pH-meter measured values.

Fig. 2 Representative MRI-CEST images of a breast tumour bearing mouse showing difference ST% contrast map (calculated as ST% after injection – ST% before injection) at 4.2 ppm (a) and at 5.5 ppm (b), respectively, pH map (c) and extravasation map (d) overlaid onto the anatomical T_{2w} -image. Pre- and post- iopamidol injection ST% curves from ROIs including the two tumours are shown in (e).

Fig. 3 Average tumour pHe values in mice drinking natural or bicarbonated water showing a statistically significant increase of tumour pHe after 5 days of bicarbonated water (a). Representative tumour pHe maps showing higher percentage of pixels with more acidic values for control mice (b) in comparison to sodium bicarbonate treated ones (c).

Fig. 4 Combined (a) PET/CT and (b) MRI T_{2w} /CEST pH images of a representative TS/A tumour bearing mouse with different ^{18}F -FDG uptake levels: PET images showing tumour area with higher ^{18}F -FDG uptake levels correspond to pH maps with lower tumour extracellular pH values. Distribution histogram plots (c) of MRI-CEST pH values within two ROIs designed in the PET image (b) for tumour regions characterised by high (ROI 1) and low (ROI 2) FDG uptake values. ROI1 shows more acidic values in comparison to ROI2 (mean pH = 6.5 ± 0.3 and 6.8 ± 0.5 for ROI1 and ROI2, respectively).

Fig. 5 Scatterplots with regression line (solid line) showing correlations between multi-modality PET/MRI calculated estimates. (a) %ID/g ^{18}F -FDG uptake as a function of extracellular tumour pH. (b) SUV ^{18}F -FDG uptake as a function of extracellular tumour pH. (c) SUV_{MAX} ^{18}F -FDG uptake as a function of extracellular tumour pH.

FIGURES

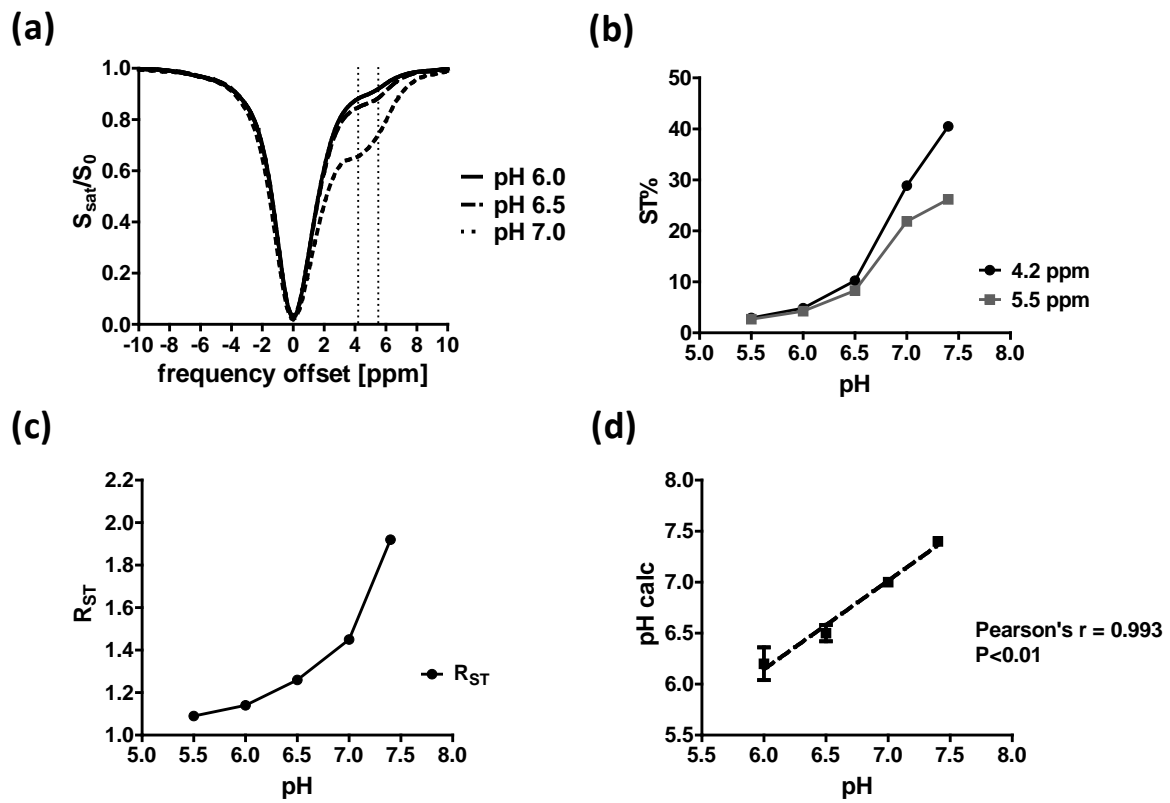


Fig. 1

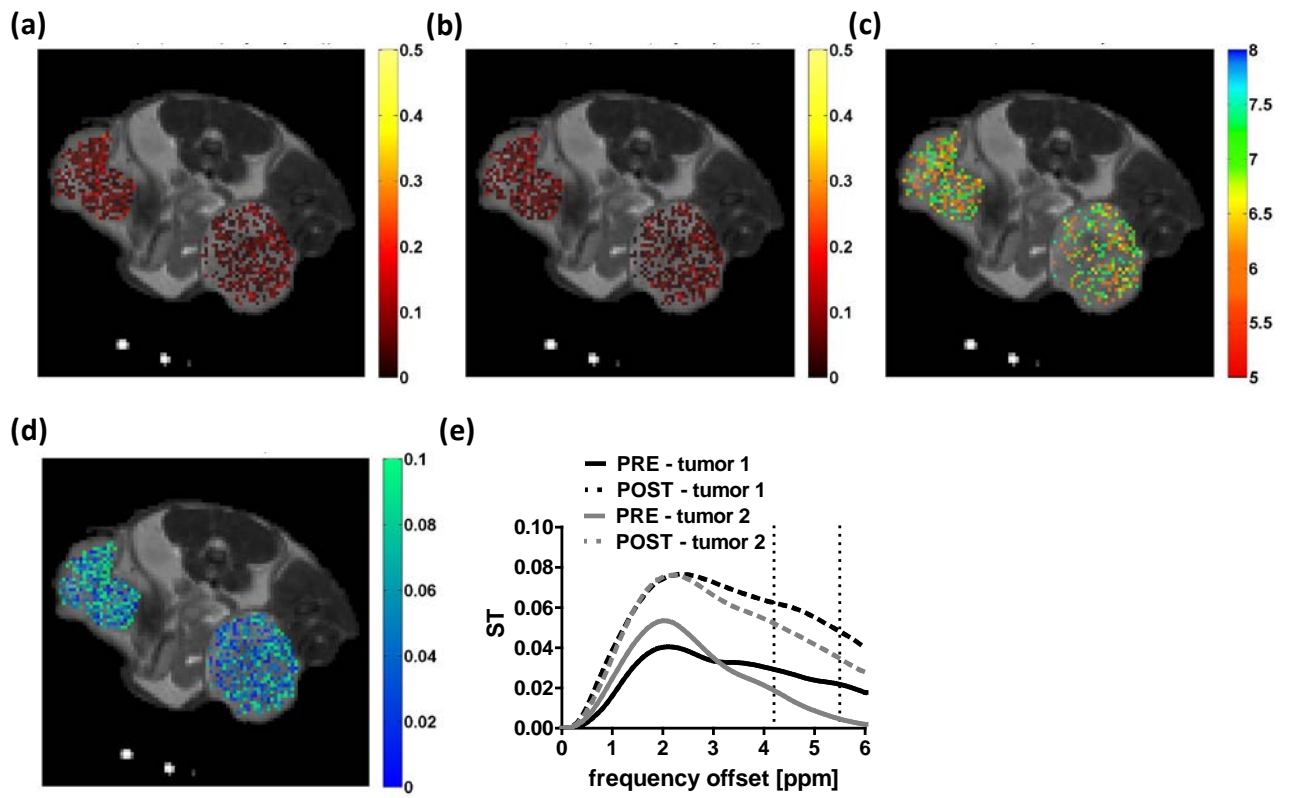


Fig. 2

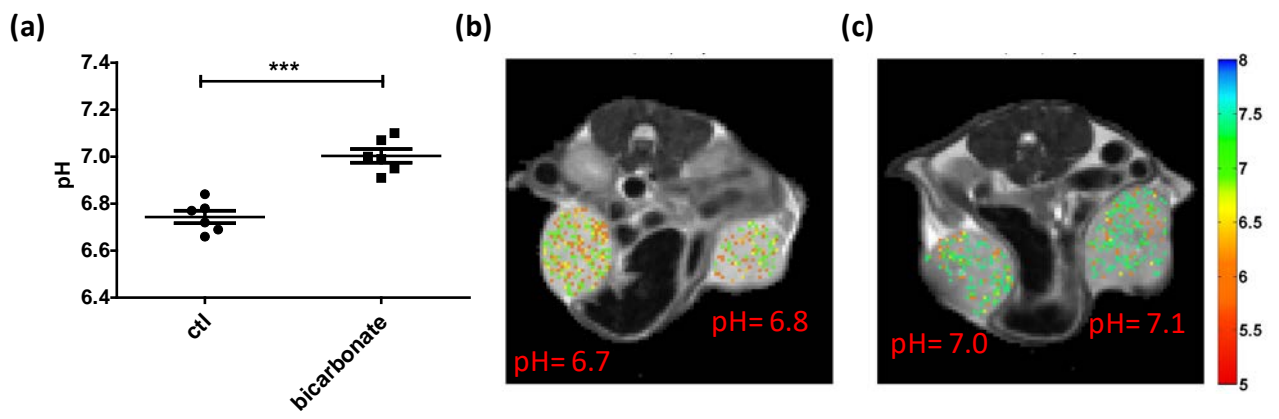


Fig. 3

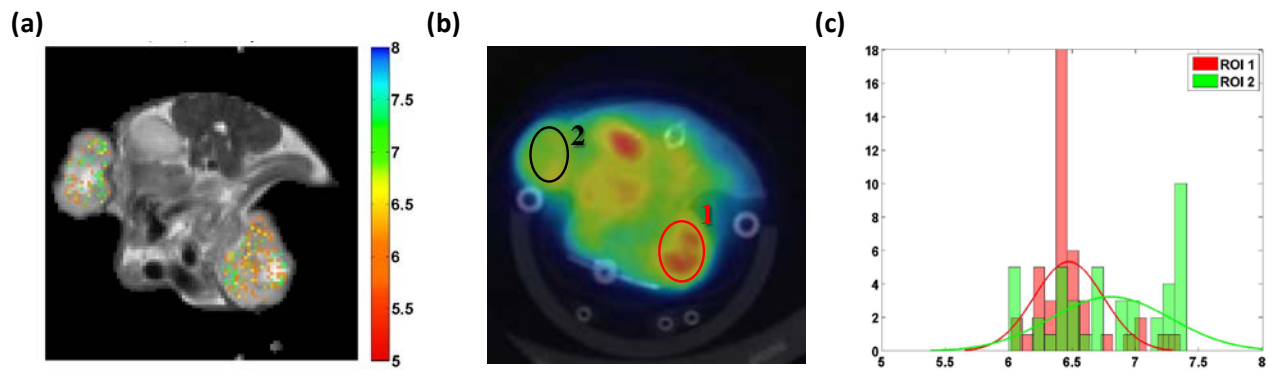


Fig. 4

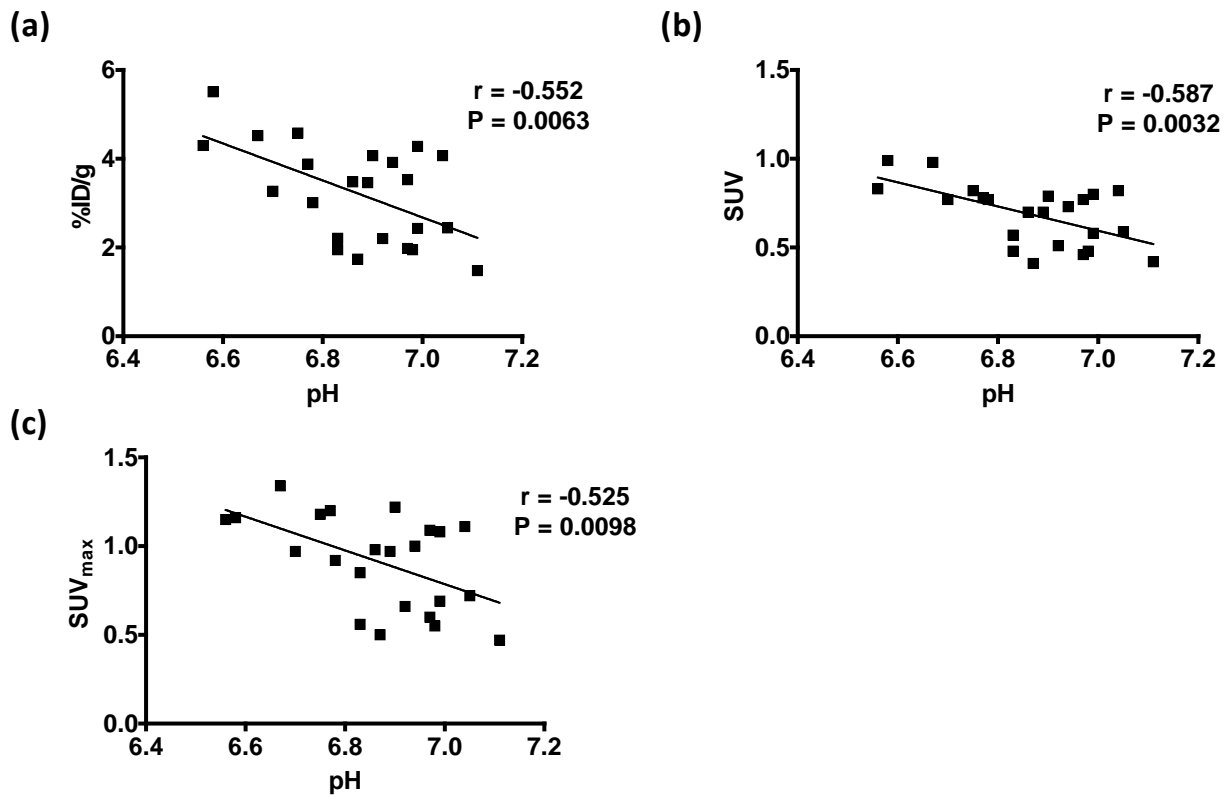


Fig. 5